Title
GISAXS Analysis for Ionomer Thin Films

Journal
ECS Transactions, 75(14)

ISSN
1938-5862

Authors
Dudenas, Peter
Kusoglu, Ahmet
Hexemer, Alex
et al.

Publication Date
2016-08-22

DOI
10.1149/07514.0643ecst

Peer reviewed

GISAXS Analysis for Ionomer Thin Films

P. Dudenas[a,b], A. Kusoglu[b], A. Hexemer[b], and A. Weber[b]

[a] Department of Chemical Engineering, University of California, Berkeley, CA 94720
[b] Lawrence Berkeley National Lab, 1 Cyclotron Road, Berkeley, CA 94720

An overview of GISAXS analysis for ionomer thin films is presented. Experimental procedures to prepare and measure thin films using GISAXS is described. Typical features of ionomer scattering images are discussed before detailing three different types of analysis which can be used in conjunction with one another to elucidate additional information from scattering patterns. Example data are provided to illustrate these techniques.

Introduction

Perfluorinated sulfonic acid ion-conducting polymers (PFSA ionomers) have been the gold standard for ion-conducting materials in fuel cells since their discovery. This is due to their combination of excellent mechanical stability and high proton conductivity, stemming from a PTFE backbone with ether side chains terminated in a sulfonic acid group. PFSA ionomers weakly phase separate, leading to a poorly ordered bi-continuous matrix of hydrophilic and hydrophobic domains (1, 2). The weak phase separation makes it inherently difficult to study morphological changes as a function of environmental conditions, and is perhaps one of the reasons the source of O_2 resistance in the catalyst layer has yet to be elucidated (3). Manufacturing low platinum loaded catalyst layers requires this resistance to be mitigated; active research is attempting to achieve this using a variety of methods (4-6). Whether this is achieved with new ionomer chemistries, new catalysts, or novel processing conditions, understanding the resulting ionomer morphology is crucial to successfully implementing these solutions.

This transaction serves as a guide for analysis of grazing incidence small angle x-ray scattering (GISAXS) of ionomer films, which goes beyond standard measures to provide additional analyses of these materials that lack strong morphological features. Standard experimental procedures and morphological features will be discussed, before moving onto three types of analysis of GISAXS scattering patterns. Standard line cuts are given a brief overview and example, while Incidence Angle Resolved GISAXS (IAR-GISAXS) and Bragg Analysis are demonstrated as an in-situ film thickness measurement and validated against ellipsometry data.

Experimental Procedures

Sample Preparation

Ionomer thin films are often prepared using drop casting, spin coating, and dip coating (7, 8). Of these three methods, drop casting is the least desirable method due to a large variation in thickness across the sample, arising from the coffee stain effect. Dip

coating can achieve good uniformity with dilute solutions, but with more concentrated solutions can suffer from the same thickness variation as drop casting. Spin coating achieves excellent film uniformity across a large range of thicknesses (5 nm-1 um) and is the preferred method of film preparation. Solution concentration, dispensed volume, coater speed, and acceleration all need to be optimized to achieve the desired thickness with good uniformity. Concentrated solutions can be purchased from chemical providers and diluted to achieve a desired thickness. Isopropanol is a good diluent, which provides film formation free of defects such as pinholes or non-uniformities. Films are typically prepared on bare silicon wafers, or wafers coated with metal like gold or platinum.

Characterization

Samples are loaded onto a sample stage and aligned with the x-ray beam with procedures unique to each beamline. The sample is then shot, as shown in Figure 1, at an incidence angle slightly above the critical angle, which allows the x-ray beam to penetrate the entire sample. Shooting close the critical angle maximizes the electric field intensity (EFI) within the film, leading to a stronger scattering pattern (9). The x-ray beam impinges on the sample and is scattered by molecules in the sample. Scattered waves are collected with an area detector. Correlated structures in the sample leads to constructive interference of waves, manifested as peaks in the scattering pattern. Peak position and shape yields information on correlation distances and degree of order within a film. In addition to the samples, it is generally recommended to take scattering patterns of blank substrates, in order to make sure scattering features are coming from the film and not the substrate itself. Substrate images may also be used for background subtraction, depending on the information desired.

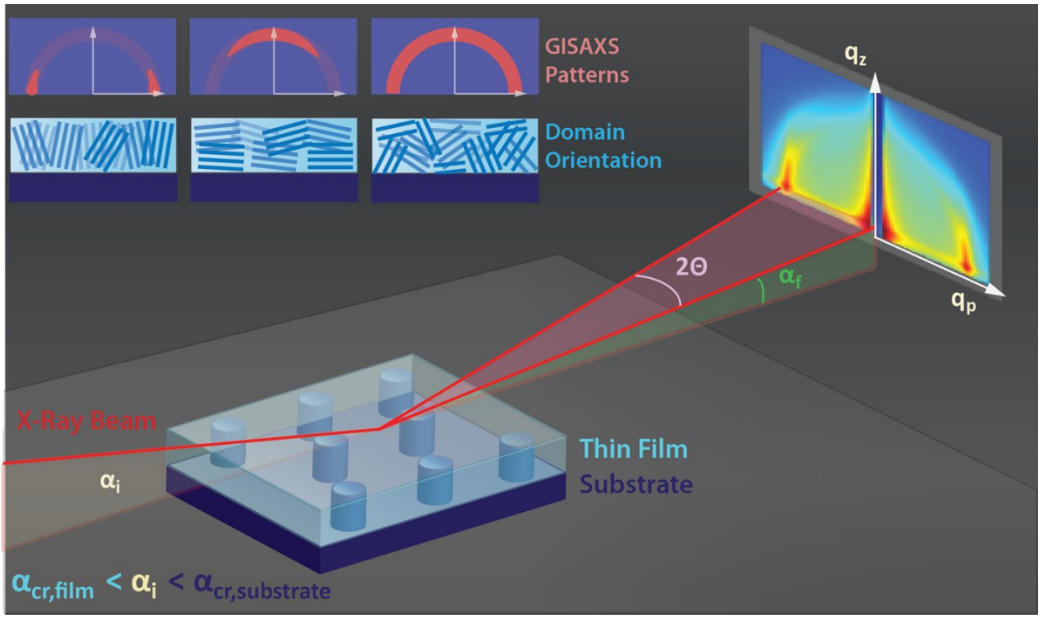

Figure 1. X-rays are shot at a grazing incidence onto the sample. Correlated domains give rise to peaks in the scattering pattern, collected by a 2D area detector. The inset patterns show examples of domain orientation and their resulting scattering patterns.

Additional Considerations Intense x-ray radiation present at synchrotron facilities is what enables high quality scattering images, but can also damage samples. Large doses of

x-ray radiation can cause chain scission, causing a loss in morphological features and noticeable marks on samples (10). Optimum exposure times minimize beam damage while still capturing all morphological features with maximum signal to noise ratio. Typical exposure times are 1-20 seconds.

Morphological Features

Ionomer Peak The hallmark scattering feature of PFSAs is the ionomer peak. Located at a d-spacing of 3-6 nm, the peak is thought to correspond to the distance between ionic domains, separated by hydrophilic backbone. Dry samples display the peak around 3 nm d-spacing, which swells upwards of 6 nm upon exposure to humidified air or liquid water. The position and shape depends on hydration, counter ion species, processing conditions, and equivalent weight. Numerous transmission x-ray studies have been performed on bulk membranes to study the response of this scattering feature (11-14).

Paracrystalline Peak The PTFE backbone is semi crystalline and will display a peak in the wide angle x-ray (WAXS) regime. In the small angle regime, a peak at approximately 10 nm d-spacing corresponds to the distance between crystallites. The intensity of the peak correlates to crystallinity in the sample, though is often absent from thin film samples because of the low crystalline content.

Diffuse Kiessig Fringes arise from the interference of x-rays reflected at the surface of a film, and x-rays reflected from within the film(15). The interference of these two reflections causes high intensity sheets in the scattered signal, and the period corresponds to the vertical distance between reflection points. Diffuse Kiessig fringes can arise from buried nanostructures or correlated roughness between the substrate and film surface.

GISAXS Analysis

Line Cuts

To generate line cuts, a vertical or horizontal section of the scattering image is taken and averaged over some small width. Vertical line cuts provide structural information through the plane of the film and horizontal line cuts provide structural information in the plane of the film, parallel to the substrate. Azimuthal line cuts are generated by plotting the scattering intensity at a constant q, as a function of angle from horizontal. These line cuts provide information on the distribution of spacing in plane vs out of plane. Peak positions indicate spacing, and by isolating the peak and calculating the full width half maximum (FWHM), the relative degree of ordering of the sample can be determined. Scattering images are reciprocal space images, and peak positions are related to real space correlation distances using Equation 1.

$$d = \frac{2\pi}{q} \qquad [1]$$

IAR-GISAXS

GISAXS images are normally taken at an incidence angle slightly above the critical angle of the film. This allows for x-rays to penetrate the entire depth of the film and maximizes the electric field intensity within the sample, which leads to higher scattering

and better signal to noise in collected images. Varying the incident angle changes the EFI distribution, which can be leveraged to extract depth information (16, 17). By shooting a set of images at small increments of the incidence angle, line cuts can be extracted from each image and stitched together to create plots as shown in Figure 2.

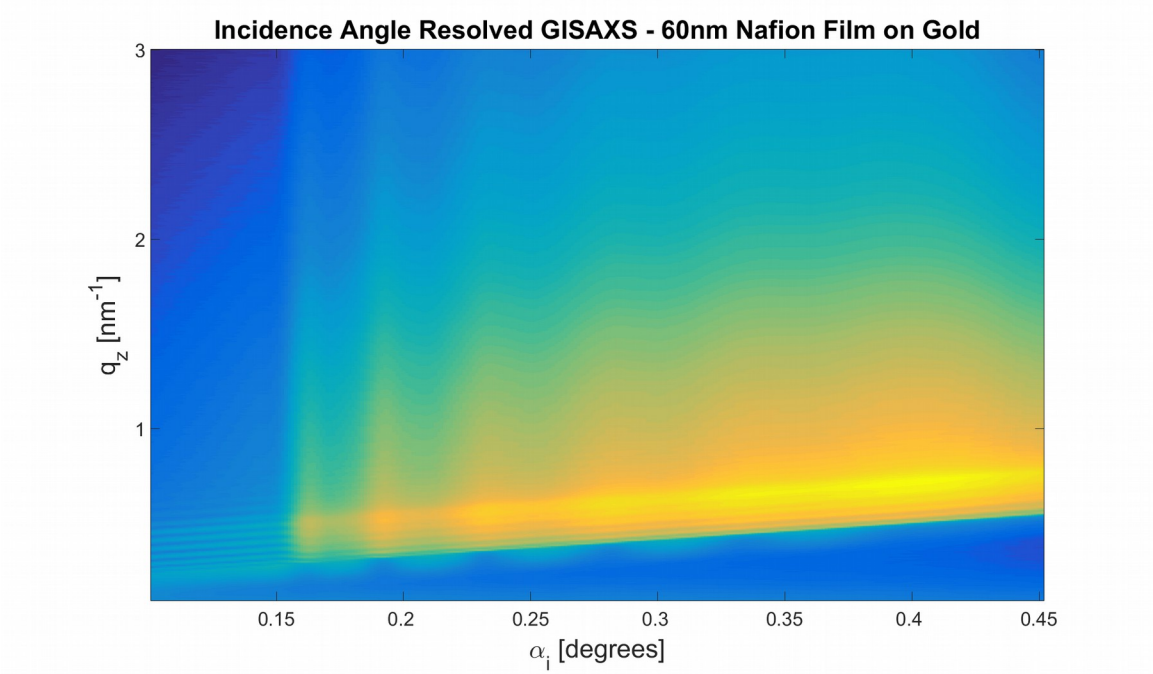

Figure 2. IAR-GISAXS plot of a 60 nm Nafion film on gold. The critical angle of the film can be seen at ~0.16 degrees.

Varying the incidence angle in this manner affects the local EFI through the depth of the film and thus allows us to highlight specific depths of the film. These plots can be used to more precisely determine the critical angle of the film, which is generally estimated based on the chemical makeup of the sample and does not take into account environmental conditions which may affect this value. From the critical angle θ_c, the index of refraction can be calculated using Equation 2. δ is the real part of the complex index of refraction.

$$\theta_c = \sqrt{2\delta} \qquad [2]$$

Bragg Analysis

The interference of x-rays that generate the diffuse Kiessig fringes obeys Bragg's law, modified for grazing incidence and refraction(18). Using Equation 3 the peak positions can be used to determine the period of interference; in the case of a single thin film, this corresponds to the film thickness.

$$m\lambda = 2 d_m \sin[\theta]\left(1 - \frac{\delta}{\sin^2\theta}\right) \qquad [3]$$

m is the peak number, lambda the x-ray wavelength, d is the period of interference, theta is the angle of the peak position, and delta is the real part of the index of refraction.

Delta can be calculated from IAR-GISAXS plots. Theta is calculated from the q value, as shown in Equation 4.

$$\theta = \tan^{-1}\left[\frac{q}{q_{px} SDD}\right] \quad [4]$$

Qpx is a conversion factor from reciprocal space to physical distance on the detector, and SDD is the sample to detector distance, calculated from a silver behenate standard.

Experimental Results

5 wt% Nafion solution, purchased from Sigma-Aldrich, was diluted with Isopropyl Alcohol (IPA) and cast on gold coated silicon substrates. A 60 nm and 180 nm film were prepared in this manner, as measured by ellipsometry. The films were each shot with x-rays at ambient conditions, and the 60 nm film was also shot under a humidified environment at 92% relative humidity.

Each sample was shot across a range of incidence angles, from 0.1 to 0.45 degrees. This is done so that linecuts from each image may be stitched together to generate IAR-GISAXS plots. The first peak in intensity with incidence angle corresponds to the critical angle of the film. Using Equation 2, the index of refraction can be calculated, which is used in Bragg Analysis. Table 1 shows the index of refraction for the two films. The critical angle of the 60 nm film does not change upon hydration, which indicates that the surface density does not change. Incorporation of water into the surface would make this region less dense and reduce the critical angle of the film. The 180 nm film has a slightly lower critical angle, indicating a less dense surface. The peak that appears at 0.5 nm^{-1} in Figure 2 and present in both samples comes from the gold substrate, not the Nafion film and highlights the importance of substrate characterization in order to avoid misidentifying scattering features

TABLE I. Index of Refraction.

Sample	Θ_c	δ
60 nm on gold	0.15564	3.724e-6
60 nm on gold (92% RH)	0.15564	3.724e-6
180 nm on gold	0.15228	3.672e-6

To perform Bragg analysis on these films, an image is chosen from the set of incidence angles that shows strong Kiessig fringes, below the critical angle of the substrate so that strong reflection occurs. An out of plane linecut is taken, and from this linecut the Kiessig fringe peaks positions are located. Figure 3a shows the linecuts for the two dry films and the difference in frequency of the Kiessig Fringes. Equation 3 is fitted to the peak numbers and positions, shown in Figure 3b, to extract d_m, the period of interference. The 60 nm film has a d_m of 70.5 nm calculated in this manner, and the 180 nm film has a d_m of 220 nm. This indicates the period of interference is the film thickness, itself.

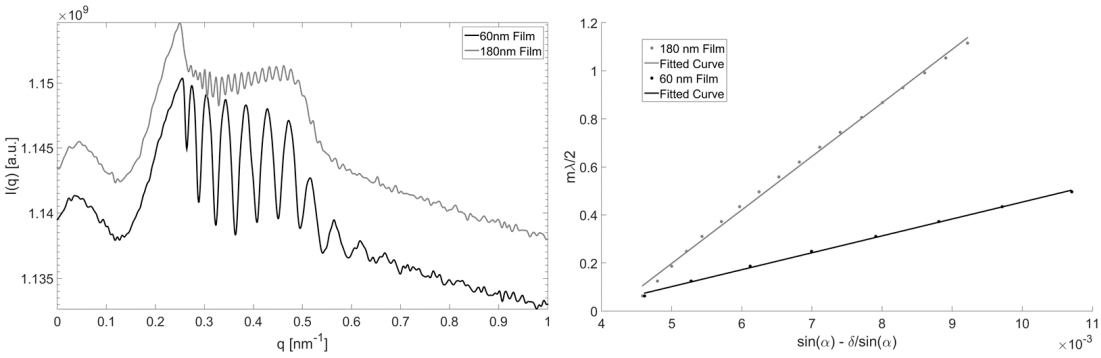

Figure 3. a) Out of plane line cuts for the 60 nm and 180 nm film. b) Peak positions fit with Equation 3. The slope of these fits is the period of interference, and corresponds to the film thickness.

Comparing the Kiessig fringes of the dry and humidified 60 nm film in Figure 4, the frequency of the fringes is higher in the hydrated film. The swelling of the film upon hydration is captured by the Bragg analysis, and demonstrates that Bragg analysis of Kiessig fringes can be used as an in-situ thickness measurement. Conformal coating of the film such that substrate features are replicated at the surface is required in order to produce diffuse Kiessig fringes (19).

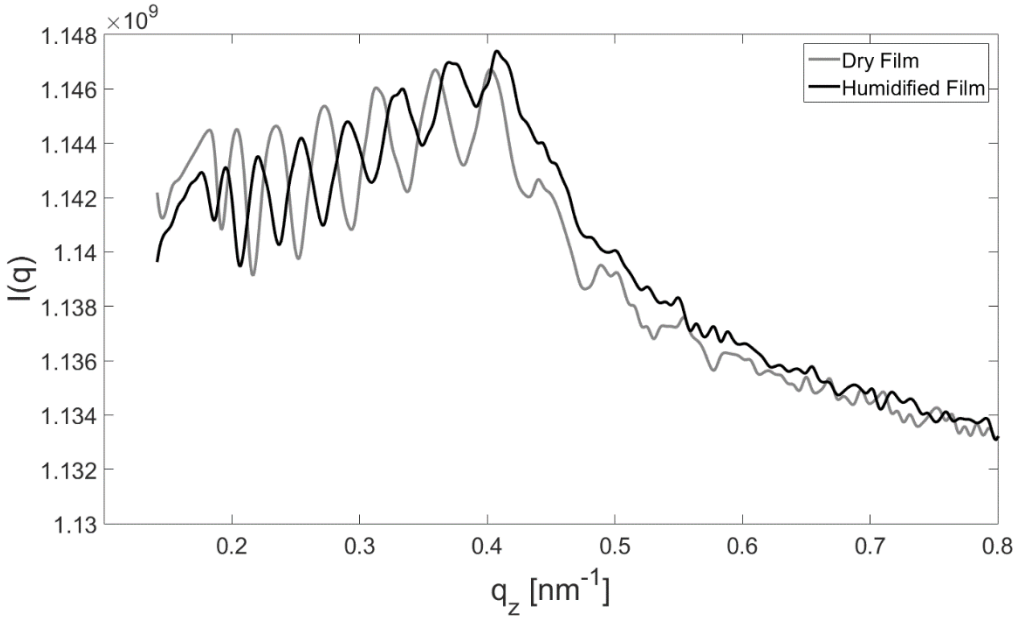

Figure 4. 60 nm Nafion film on gold, dry and humidified. The increased frequency of the Kiessig fringes correlates to the increased film thickness upon water uptake. Bragg analysis of the humidified film yields a d_m of 77 nm.

Conclusion

GISAXS analysis is detailed for ionomer thin films, starting from sample preparation and characterization. The ionomer peak, paracrystalline peak, and diffuse Kiessig Fringes are discussed before moving onto the analysis of scattering images. Correlation distances and ordering can be extracted from line cuts. Incidence angle scans are used to generate IAR-GISAXS plots, which show depth sensitive information and allow the calculation of the index of refraction. The index of refraction does not change upon hydration, which lends credence to the theory of a "skin" layer existing. This index of refraction is also used in Bragg analysis, which is demonstrated as a method of in situ film thickness measurement. One can imagine that in future materials, such as an ionomer composite, IAR-GISAXS and Bragg analysis can be used in conjunction to study depth dependent features or layering induced in such a material.

Acknowledgments

This work was funded by the Assistant Secretary for Energy Efficiency and Renewable Energy, Fuel Cell Technologies Office, of the U. S. Department of Energy under Contract No. DE-AC02-05CH11231 and by the Army Research Office under award number AWD00000675. Beamline 7.3.3 of the Advanced Light Source is supported by the Director of the Office of Science, Office of Basic Energy Sciences, of the U.S. Department of Energy under Contract No. DE-AC02-05CH11231.

References

1. K. A. Mauritz and R. B. Moore, *Chemical reviews*, **104**, 4535 (2004).
2. F. I. Allen, L. R. Comolli, A. Kusoglu, M. A. Modestino, A. M. Minor and A. Z. Weber, *ACS Macro Letters*, **4**, 1 (2014).
3. A. Z. Weber and A. Kusoglu, *J. Mater. Chem. A*, **2**, 17207 (2014).
4. H. Chen, J. D. Snyder and Y. A. Elabd, *Macromolecules*, **41**, 128 (2008).
5. C. Wang, M. Waje, X. Wang, J. M. Tang, R. C. Haddon and Yan, *Nano letters*, **4**, 345 (2004).
6. B. Wang, *Journal of Power Sources*, **152**, 1 (2005).
7. D. K. Paul, K. Karan, A. Docoslis, J. B. Giorgi and J. Pearce, *Macromolecules*, **46**, 3461 (2013).
8. M. A. Modestino, D. K. Paul, S. Dishari, S. A. Petrina, F. I. Allen, M. A. Hickner, K. Karan, R. A. Segalman and A. Z. Weber, *Macromolecules*, **46**, 867 (2013).
9. G. H. Vineyard, *Physical Review B*, **26**, 4146 (1982).
10. S. A. Vaselabadi, D. Shakarisaz, P. Ruchhoeft, J. Strzalka and G. E. Stein, *Journal of Polymer Science Part B: Polymer Physics*, **54**, 1074 (2016).
11. A. Kusoglu, M. A. Modestino, A. Hexemer, R. A. Segalman and A. Z. Weber, *ACS Macro Letters*, **1**, 33 (2012).
12. T. D. Gierke, G. E. Munn and F. C. Wilson, *Journal of Polymer Science: Polymer Physics Edition*, **19**, 1687 (1981).
13. M. Fujimura, T. Hashimoto and H. Kawai, *Macromolecules*, **14**, 1309 (1981).
14. J. A. Elliott, S. Hanna, A. M. S. Elliott and G. E. Cooley, *Macromolecules*, **33**, 4161 (2000).

15. I. Pape, T. P. A. Hase, B. K. Tanner and M. Wormington, *Physica B: Condensed Matter*, **253**, 278 (1998).
16. M. A. Singh and M. N. Groves, *Acta Crystallographica Section A: Foundations of Crystallography*, **65**, 190 (2009).
17. B. Lee, C.-T. Lo, P. Thiyagarajan, D. R. Lee, Z. Niu and Q. Wang, *Journal of Applied Crystallography*, **41**, 134 (2008).
18. Q. Yang and L. R. Zhao, *Materials Characterization*, **59**, 1285 (2008).
19. P. Müller-Buschbaum and M. Stamm, *Macromolecules*, **31**, 3686 (1998).